Infrared surface plasmons in two-dimensional silver nanoparticle arrays in silicon

H. Mertens,[a] J. Verhoeven, and A. Polman
FOM-Institute AMOLF, Kruislaan 407, 1098 SJ Amsterdam, The Netherlands

F. D. Tichelaar
National Center for HREM, Rotterdamseweg 137, 2628 AL Delft, The Netherlands

(Received 15 March 2004; accepted 16 June 2004)

We present two-dimensional arrays of silver nanoparticles embedded in amorphous silicon, fabricated by a sequential Si/Ag/Si electron-beam evaporation process. The particle arrays exhibit surface plasmon resonance spectra in the near-infrared (0.9 eV), with tails extending below 0.5 eV. The data are compared with calculations that take into account measured particle size, shape anisotropy, and separation. It is concluded that the large redshift is mainly due to the high refractive index of the matrix, with shape anisotropy and interparticle coupling contributing several tenths of an electron volt. This work enables plasmon-related applications at the telecommunication wavelength of 1.5 μm (0.8 eV). © *2004 American Institute of Physics*. [DOI: 10.1063/1.1784542]

Metal nanoparticles have been the subject of extensive research for many years because of their anomalous electromagnetic properties originating from the resonant interaction between light and collective conduction electron oscillations, so-called surface plasmons.[1,2] These properties, in particular local electric field enhancements, enable applications such as single molecule detection using surface-enhanced Raman scattering[3] and the synthesis of composite materials exhibiting an enhanced nonlinear optical response.[4] In addition, resonant energy transfer between closely spaced metal nanoparticles enables transport of electromagnetic energy at length scales below the diffraction limit.[5]

Since all these applications rely on the resonant behavior of localized surface plasmons, they are restricted to a limited frequency range determined by the dielectric functions of the involved media, the size and shape of the particles, and the electromagnetic interaction between them.[1] For composites consisting of isolated spherical noble-metal nanoparticles embedded in glass, constituting the most extensively investigated metallo-dielectric materials, the surface plasmon resonances occur in the visible regime. In order to employ localized surface plasmon properties in the near-infrared, e.g., for telecommunication, a number of methods have been investigated to lower the resonance frequency: using high-index matrices such as GaAs[6] or TiO_2,[7] applying nanolithography to define anisotropically shaped nanoparticles,[8] and aligning nanoparticles to induce electromagnetic interaction, by methods such as nanolithography[9] or ion irradiation.[10] In this letter, we report on the experimental realization of two-dimensional silver nanoparticle arrays embedded in amorphous silicon (*a*-Si), in which these three mechanisms (i.e., high-index matrix, anisotropically shaped nanoparticles, and interparticle coupling) are combined to shift the surface plasmon resonance spectrum well into the near-infrared, peaking at 0.9 eV(1.4 μm), with tails below 0.5 eV(2.5 μm).

Two-dimensional Ag nanoparticle arrays embedded in *a*-Si were fabricated by sequential Si/Ag/Si electron-beam evaporation on both glass and NaCl substrates, resulting in samples as schematically illustrated in Fig. 1(a). The Ag depositions were varied in duration in order to fabricate samples with evaporated Ag thicknesses of 0.6, 1.0, and 2.2 nm, respectively, as was monitored *in situ* using a crystal thickness monitor and verified afterwards by Rutherford backscattering spectrometry (RBS). Ag nanoparticles formed during deposition by Volmer-Weber type growth, and surface plasmon resonances were observed in samples made using deposition rates $\leqslant$0.05 nm/min. For all samples, the Ag nanoparticles were positioned in the center of a 14-nm-thick *a*-Si layer by performing the Ag deposition in between two separate *a*-Si depositions. After each *a*-Si deposition, 300 eV Kr ion etching was applied to reduce the surface roughness to ~0.3 nm.[11] X-ray reflectometry was used to monitor the *a*-Si thickness during both deposition and etching steps. The substrates were kept at room temperature throughout the entire process.

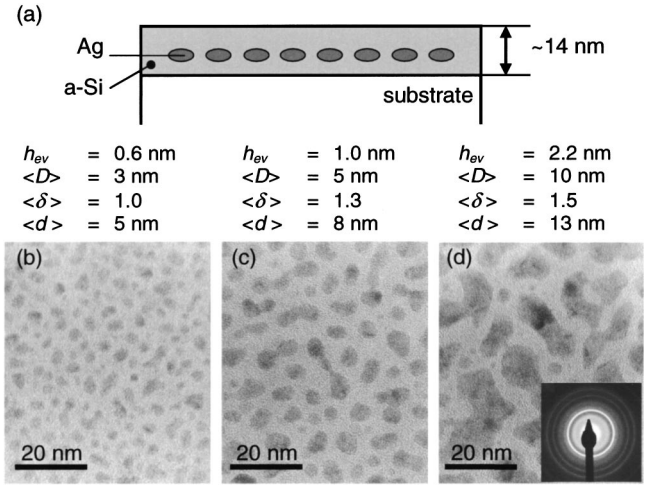

FIG. 1. (a) Schematic representation of the sample geometry, and (b)–(d) plan-view bright-field TEM images of the Ag nanoparticle arrays embedded in *a*-Si prepared with (b) 0.6 nm, (c) 1.0 nm, and (d) 2.2 nm Ag, respectively. Evaporated silver thickness (h_{ev}), mean equivalent diameter ($\langle D \rangle$), mean aspect ratio ($\langle \delta \rangle$), and mean interparticle spacing ($\langle d \rangle$) are indicated for each sample. The inset in (d) shows a SADP pattern, revealing the crystalline structure of the Ag nanoparticles.

[a]Electronic mail: mertens@amolf.nl

The thin films deposited on NaCl were used to investigate the shape, size, and separation of the Ag nanoparticles by plan-view transmission electron microscopy (TEM). For this purpose, the Si/Ag/Si films were separated from the NaCl in water and subsequently put on carbon-coated copper grids. A Philips CM30T and a Philips CM30UT-FEG electron microscope, operated at 300 keV, were used to take bright-field images, high-resolution images, and selected-area diffraction patterns (SADP). Elemental composition was investigated by energy-dispersive spectroscopy (EDS). Optical transmittance T and specular reflectance R were measured at normal incidence in the energy range 0.5–4 eV with a Perkin-Elmer Lambda 900 spectrophotometer for the samples deposited on glass. Absorptance A was calculated from: $A=1-T-R$, neglecting diffuse scattering.

Figures 1(b)–1(d) show plan-view bright-field TEM images of the Ag-containing samples. Clearly distinguishable nanoparticles can be observed. EDS on a large particle confirmed the composition to be Ag. The TEM images reveal that increasing the evaporated Ag thickness leads to larger particle sizes. Quite irregular shapes can be observed for the large particles in Fig. 1(d). SADP patterns, one of which is displayed in the inset of Fig. 1(d), show rings indicating the presence of finely dispersed crystalline material (sharp rings) and amorphous material (broad rings). The sharp rings are found to correspond to crystalline Ag lattice spacings, while the broad rings are mainly attributed to *a*-Si. The crystalline structure of the Ag nanoparticles is confirmed in HREM images (not shown), in which multiple crystals can be recognized in each nanoparticle.

Characteristic parameters for the three sample topologies are listed in Figs. 1(b)–1(d). The Ag areal density has been measured by RBS with an accuracy better than 5%. Subsequently, the evaporated Ag thickness h_{ev} has been derived from the areal density by using the bulk density for Ag; the mean in-plane equivalent particle diameter $\langle D\rangle$ from TEM, where D is defined as the diameter of a circle with the same in-plane area as the particle under consideration. Combining h_{ev} with the areal particle density, the characteristic particle height h_{ob}, was determined by assuming an oblate ellipsoidal shape. The mean particle aspect ratio $\langle\delta\rangle$ (major over minor diameter) increases from 1.0 (spherical particles) for the thinnest film to 1.5 for the thickest film. The mean center-to-center interparticle spacing $\langle d\rangle$ increases from 5 to 13 nm. These numbers indicate that significant particle coarsening occurred for the thicker films.

Figure 2(a) shows the optical absorptance spectra for all three Ag evaporated samples and a reference sample without Ag. The latter shows a broad feature above 1.5 eV, due to the intrinsic band-to-band absorption in *a*-Si. The samples with Ag exhibit additional absorptance, mainly at energies below 2.5 eV, which is attributed to the surface plasmon absorption by the Ag nanoparticles. This contribution is more clearly shown in Fig. 2(b) in which absorption by *a*-Si has been corrected for. The surface plasmon absorptance spectrum is shown to be rather broad (~1 eV full width at half-maximum), and increases in magnitude and shifts toward lower energies for increasing Ag content. The absorptance peak energies are plotted versus evaporated Ag thickness in Fig. 3 (closed squares).

In order to calculate the relative importance of the mechanisms contributing to the redshift of the surface plasmon resonance, we first evaluate the effect of shape anisotropy and refractive index of the matrix. The ensemble-averaged resonance frequency was obtained by averaging the calculated plasmon resonance frequencies of a large number of particles (103, 98, and 48, for the 0.6, 1.0, and 2.2 nm depositions, respectively) taking the TEM data (shape anisotropy and volume) as input. Each particle i was approximated as an oblate with minor axis h_{ob} and major axes equal to D_i.

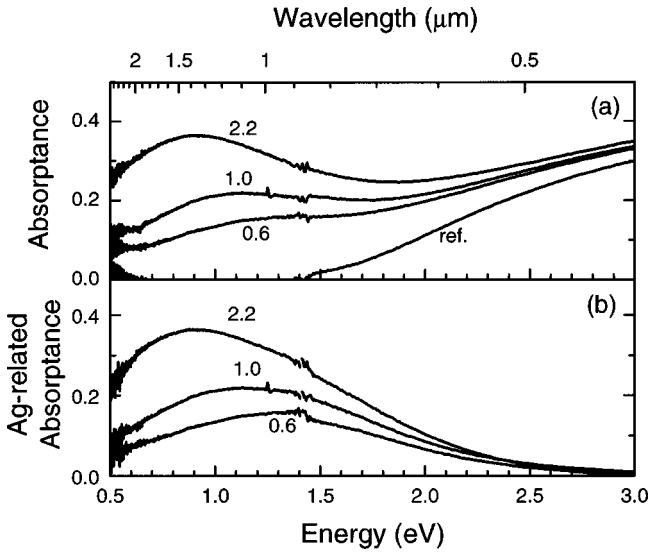

FIG. 2. Optical absorptance spectra of Ag nanoparticle arrays embedded in *a*-Si: (a) raw data, (b) Ag-related absorptance. The evaporated Ag thicknesses are indicated in nm. The surface plasmon absorption peak increases in magnitude and shifts toward lower energies for increasing Ag content.

The surface plasmon resonance frequency $\omega_{0,i}$ of nanoparticle i, found by evaluating the resonance condition of its polarizability in the quasistatic limit,[1] is described by

$$\omega_{0,i}=\omega_p\sqrt{\frac{L_i}{\varepsilon_m-L_i(\varepsilon_m-\varepsilon_\infty)}}, \tag{1}$$

with $\varepsilon_m=n_m^2$ the dielectric constant of the embedding medium, L_i a geometrical factor determined by the aspect ratio δ_i^2, and ε_∞ and ω_p parameters of a modified Drude model for the real part of the dielectric function of Ag: $\varepsilon'(\omega)=\varepsilon_\infty-(\omega_p/\omega)^2$, determined by fitting the model to experimental

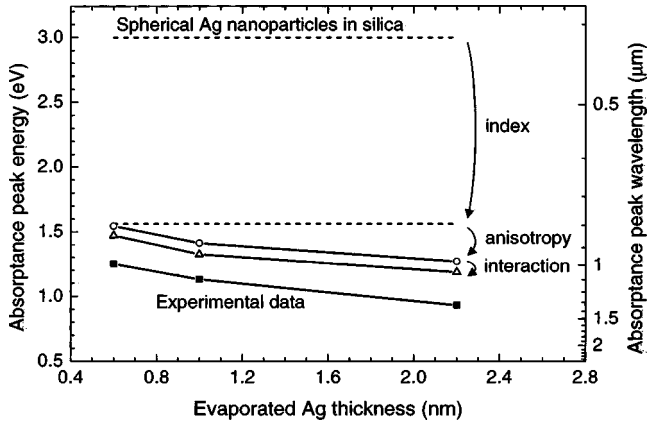

FIG. 3. Calculated (open circles and triangles) and experimental (closed squares) absorptance peak energies for Ag nanoparticle arrays in *a*-Si. The resonance energy for spherical Ag nanoparticles in silica glass is indicated for reference. The three mechanisms contributing to the redshift are indicated.

data for Ag.[12] The refractive index of the *a*-Si matrix n_m determined from transmittance and reflectance measurements of the reference sample without Ag and found to be 3.7 in the spectral range under consideration. For nanoparticles embedded in the center of a 14-nm-thick *a*-Si layer, it is appropriate to use this bulk value for the refractive index of the matrix.[13] The average absorptance peak frequency ω_{peak} was calculated by summing over the particle ensembles taking into account the oscillator strength for each particle using its volume as a normalization factor.

The open circles in Fig. 3 show the calculated absorptance peak energies ($\hbar\omega_{\text{peak}}$) for the three nanoparticle ensembles embedded in *a*-Si. Data for the surface plasmon resonance energy of Ag nanoparticles in silica glass (index 1.46) are shown for reference. Clearly, the largest contribution to the redshift is due to the high refractive index of the *a*-Si matrix compared to silica. The anisotropy for the 1.0 and 2.2 nm films adds another 0.2–0.3 eV to the redshift.

To model the influence of interparticle coupling, the nanoparticles were considered as ideal dipoles that are coupled by near-field interaction. Under the assumption that the dipoles are oscillating in phase (far-field excitation), the resonance frequency of nanoparticle *i* is given by

$$\omega_i = \sqrt{\omega_{0,i}^2 - \frac{\omega_p^2}{4\pi\varepsilon_m}\sum_{j\neq i}\frac{V_j(3\cos\theta_{i,j}-1)}{d_{i,j}^3}}, \qquad (2)$$

where $\omega_{0,i}$ is the resonance frequency if there would be no interaction, as described by Eq. (1), and $\theta_{i,j}$ the angle between the orientation of the dipoles (i.e., incident polarization) and the interparticle axis. In this summation we have taken the particle coordinates derived from TEM as input parameters (evaluating the same particles as in the analysis above). Only particles *j*, with volume V_j at distance $d_{i,j}$ from particle *i*, with $d_{i,j}<30$ nm were taken into account, as coupling is negligible for larger distances. By averaging over the particle ensembles, the absorptance peak energies ($\hbar\omega_{\text{peak}}$) are derived as plotted in Fig. 3 (open triangles). As can be seen, interparticle coupling adds a relatively small redshift of ~0.1 eV.

Comparing the experimental data to the calculation, a discrepancy of ~0.2 eV is observed for all samples. This may be due to inaccuracies in the optical data for Ag and *a*-Si, and to the approximations of oblate-shaped particles and resonantly interacting ideal dipoles in our model. Finite-difference time-domain calculations of the relaxation of excited nanoparticle ensembles could be used to remove the necessity of making these approximations. Note that the calculated contribution of shape anisotropy (the decreasing trend with increasing thickness in Fig. 3) is in good agreement with the experiment.

The bandwidth of the measured absorptance peak (~1 eV) is significantly larger than the homogeneous linewidth of surface plasmon resonances in Ag nanoparticles (0.2–0.3 eV).[1] Possible causes are the presence of optical inhomogeneities in the *a*-Si matrix[13] and variations in particle shape and orientation.

In conclusion, we have shown that a sequential Si/Ag/Si electron-beam evaporation process enables the fabrication of two-dimensional Ag nanoparticle arrays that exhibit surface plasmon resonances in the near-infrared. A model is described for the ensemble-averaged plasmon absorption, with experimentally determined Ag nanoparticle size and shape as input, Taking into account the refractive index of the matrix, shape anisotropy, and interparticle coupling, the experimental data are quite well described. It is concluded that the main origin of the plasmon shift (~1.5 eV), regarding spherical Ag nanoparticles in silica as a reference, is the high refractive index of the *a*-Si matrix; shape anisotropy ($\langle\delta\rangle$ up to 1.5) contributes another 0.2–0.3 eV, while the influence of coupling effects is limited to ~0.1 eV. The data indicate that an increased Ag deposition thickness leads to larger shape anisotropy and thus larger plasmon redshift. By further increasing the Ag layer thickness even larger plasmon redshifts may thus be observed. The achievement of infrared surface plasmons in silicon now enables the use of electromagnetic field enhancements, surface-enhanced Raman scattering, spontaneous emission enhancement, nanoscale energy transfer, and several other plasmon-related applications at the important telecommunication wavelength of 1.5 μm.

Kobus Kuipers and Jan van der Elsken are acknowledged for stimulating discussions. This work is part of the research program of the Foundation for Fundamental Research on Matter (FOM), which is financially supported by the Dutch Organization for Scientific Research (NWO).

[1] U. Kreibig and M. Vollmer, *Optical Properties of Metal Clusters* (Springer, Berlin, 1995).
[2] C. F. Bohren and D. R. Huffman, *Absorption and Scattering of Light by Small Particles* (Wiley, New York, 1983).
[3] K. Kneipp, Y. Wang, H. Kneipp, L. T. Perelman, I. Itzkan, R. R. Dasari, and M. S. Feld, Phys. Rev. Lett. **78**, 1667 (1997).
[4] D. Ricard, P. Roussignol, and C. Flytzanis, Opt. Lett. **10**, 511 (1985).
[5] S. A. Maier, P. G. Kik, H. A. Atwater, S. Meltzer, E. Harel, B. E. Koel, and A. A. G. Requicha, Nat. Mater. **2**, 229 (2003).
[6] D. D. Nolte, J. Appl. Phys. **76**, 3740 (1994).
[7] G. Xu, M. Tazawa, P. Jin, S. Nakao, and K. Yoshimura, Appl. Phys. Lett. **82**, 381 (2003).
[8] T. R. Jensen, M. D. Malinsky, C. L. Haynes, and R. P. Van Duyne, J. Phys. Chem. B **104**, 10549 (2000).
[9] W. Rechberger, A. Hohenau, A. Leitner, J. R. Krenn, B. Lamprecht, F. R. Aussenegg, Opt. Commun. **220**, 137 (2003).
[10] J. J. Penninkhof, A. Polman, L. A. Sweatlock, S. A. Maier, H. A. Atwater, A. M. Vredenberg, and B. J. Kooi, Appl. Phys. Lett. **83**, 4137 (2003).
[11] R. Schlatmann, C. Lu, J. Verhoeven, F. J. Puik, and M. J. van der Wiel, Appl. Surf. Sci. **78**, 147 (1994).
[12] *Handbook of Optical Constants of Solids*, edited by E. D. Palik (Academic, Orlando, FL, 1985).
[13] O. Steazel, A. Stendal, M. Röder, and C. von Borczyskowski, Pure Appl. Opt. **6**, 577 (1997).